

Decoupling the catalytic and degradation mechanisms of cobalt active sites during acidic water oxidation

Received: 30 July 2024

Accepted: 9 June 2025

Published online: 16 July 2025

 Check for updates

Darcy Simondson¹, Marc F. Tesch²✉, Ioannis Spanos², Travis E. Jones³, Jining Guo¹, Brittany V. Kerr⁴, Manjunath Chatti¹, Shannon A. Bonke⁵, Ronny Golnak⁶, Bernt Johannessen^{7,8}, Jie Xiao⁶, Douglas R. MacFarlane¹, Rosalie K. Hocking^{4,9}✉ & Alexandr N. Simonov¹✉

Advancement of iridium-free catalysts for the low-pH oxygen evolution reaction (OER) is required to enable multi-gigawatt-scale proton-exchange water electrolysis. Cobalt-based materials might address this requirement, but little is known about the mechanism of operation of these OER catalysts at low pH. Here we investigate the nature and evolution of the active cobalt sites along with charge- and mass-transfer processes that support their catalytic function within a cobalt–iron–lead oxide material using in situ spectroscopic, gravimetric and electrochemical techniques. We demonstrate that corrosion of the cobalt sites and their reformation through electrooxidation of dissolved Co^{2+} do not affect the catalytic mechanism and are decoupled from the OER. The OER-coupled charge transfer is supported by $\text{Co}^{(3+\delta)+}$ -oxo-species, which are structurally different from those reported for alkaline/near-neutral conditions and are formed on a relatively slow timescale of minutes. These mechanistic insights might assist in developing genuinely practical catalysts for this vital technology.

Proton-exchange water electrolyzers use anodes containing iridium catalysts^{1,2}, which sustain the oxygen evolution reaction (OER) while remaining stable under oxidative potentials, low pH and elevated temperatures. However, the amount of iridium directly available to humanity is insufficient for scaling up the technology to the multi-gigawatt level¹. Cobalt-based catalysts present one viable alternative to the iridium-based anodes but are insufficiently stable³.

To stabilize low-pH OER catalysts with cobalt active sites, several methodologies were explored: incorporation of stabilizing elements within catalytically active Co_3O_4 (refs. 4–6), functionalization of cobalt

oxides with nanometre-scale stabilizing layers^{7,8} and doping of CoO_x active sites within acid-stable oxide matrices^{9–13}. Notwithstanding stability improvements achieved, loss of the catalytically active cobalt component was consistently observed, both in studies with aqueous electrolyte solutions and within electrolyser devices using polymer electrolytes.

It is important to recognize that all cobalt and other metal oxide catalysts, including iridium-based ones¹⁴, undergo corrosion during the low-pH OER. Thus, the reported quasi-stable operation is commonly sustained by an equilibrium between the dissolved metal and solid

¹School of Chemistry, Monash University, Clayton, Victoria, Australia. ²Max Planck Institute for Chemical Energy Conversion, Mülheim an der Ruhr, Germany. ³Los Alamos National Laboratory Theoretical Division, Los Alamos, NM, USA. ⁴Department of Chemistry and Biotechnology, Swinburne University of Technology, Hawthorn, Victoria, Australia. ⁵Yusuf Hamied Department of Chemistry, University of Cambridge, Cambridge, UK.

⁶Helmholtz-Zentrum Berlin für Materialien und Energie, Berlin, Germany. ⁷Australian Synchrotron, ANSTO, Clayton, Victoria, Australia. ⁸Institute for Superconducting and Electronic Materials, University of Wollongong, Wollongong, New South Wales, Australia. ⁹Department of Mechanical and Production Design Engineering, Surface Engineering for Advanced Materials (SEAM), Swinburne University of Technology, Hawthorn, Victoria, Australia.

✉e-mail: marc.tesch@cec.mpg.de; rhocking@swin.edu.au; alexandr.simonov@monash.edu

oxides on the electrode. This is corroborated by studies where catalyst precursors were intentionally added to the electrolyte solutions to facilitate reformation of active sites by electrooxidative deposition^{15–18}. The stabilizing effects of dissolved Co^{2+} were demonstrated for a mono-metallic cobalt oxide¹⁵ and for a more stable cobalt–iron–lead oxide system, $[\text{Co-Fe-Pb}]_x\text{O}_x$ (refs. 16,19). Substantial improvements in stability are possible with micromolar concentrations of Co^{2+} (ref. 19), which is comparable to concentrations resulting from the corrosion of non-noble-metal catalysts during acidic OER both in aqueous electrolyte solutions and PEMWE^{4,5,13}.

Thus, the OER catalysis and dissolution of the cobalt-based catalytic materials occur in parallel even for the best-performing systems^{4,5,13,20}. Given that the developments of such catalysts have only recently achieved notable progress, little is known on the mechanisms of their catalytic function and reconstruction during the reaction. This contrasts more established fields of the near-neutral and alkaline OER^{21–25}, and iridium-catalysed acidic OER^{26–29}, where in situ spectroscopic and computational techniques were used to explain the activity and stability trends. This knowledge is instrumental in the development of water electrolysis technologies but is currently missing for the emerging field of the noble-metal-free low-pH OER catalysts.

Aiming to address this, here we investigate the mechanism of the cobalt-catalysed acidic OER, using the $[\text{Co-Fe-Pb}]_x\text{O}_x$ system as an archetypal example that exhibits both sufficient stability and capability to reform by oxidative electrodeposition during operation. Interplay of corrosion and catalytically relevant redox transformations was probed by steady-state and potentiodynamic in situ X-ray absorption spectroscopy (XAS) at the cobalt K- and $L_{2,3}$ -edges, Fourier-transformed (FT) alternating current (a.c.) voltammetry (FTacv)³⁰ and electrochemical quartz crystal microbalance (eQCM).

Catalyst formation, performance and structure

The $[\text{Co-Fe-Pb}]_x\text{O}_x$ catalyst is generated by electrooxidation of acidic solutions containing the metal precursors at potentials sufficiently positive to initiate the OER¹⁶. This reproducible procedure is applicable to various electrodes, including fluorine-doped tin(IV) oxide (FTO), Au-coated quartz crystals, carbon fibre paper (CFP) and Au-coated Si_3N_4 required for different techniques employed herein (Supplementary Figs. 1 and 2 and Supplementary Table 1).

FTacv and eQCM studies of the processes involved in the $[\text{Co-Fe-Pb}]_x\text{O}_x$ formation demonstrate that electrodeposition of the catalytically active material is preceded by generation of highly-oxidized cobalt species, most likely cobalt(IV) based (Supplementary Note 1 and Supplementary Figs. 3–12). Such species would be formed on any OER anode operating in the presence of dissolved cobalt species, which are ubiquitously produced during operation of Co-based water oxidation catalysts. Indeed, corrosion of $[\text{Co-Fe-Pb}]_x\text{O}_x$ in PEMWE fed with pure water was detected herein, however, the performance stabilized after 100 h of testing at 1 A cm^{-2} and 80°C (Supplementary Note 2 and Supplementary Fig. 13). The corresponding stability (S)-number¹⁴ representing the ratio of the amount of oxygen evolved to the amount of metal dissolved was $\sim 10^8$, that is, only one order of magnitude lower than for IrO_x (ref. 31).

Previous ex situ X-ray diffraction and XAS studies concluded that $[\text{Co-Fe-Pb}]_x\text{O}_x$ adopts a crystal structure of $\beta\text{-PbO}_2$ doped with cobalt and iron^{16,19}. This interpretation is consistent with the lack of long-range order beyond $\sim 2\text{ Å}$ in the FT of the ex situ Co K-edge extended X-ray absorption fine structure (EXAFS) spectrum reported here (Supplementary Note 3 and Supplementary Fig. 14b). In situ Pb $L_{3\text{-edge}}$, Fe K- and Fe $L_{2,3\text{-edge}}$ XAS data showed no response to potential indicating that these metal sites are not directly involved in the OER catalysis (Supplementary Note 4 and Supplementary Figs. 15 and 16). As suggested before^{16,19}, the role of iron and lead is limited to facilitating the initial electrodeposition and stabilization of cobalt oxo-species—the key catalytically active sites. Among all cobalt oxo-species present within

the $[\text{Co-Fe-Pb}]_x\text{O}_x$ films examined herein, at least 15–25% were redox active (Supplementary Note 4 and Supplementary Fig. 17).

In what follows, we explored changes in the cobalt oxo-species during the OER in acidic electrolyte ($0.1\text{ M H}_2\text{SO}_4$). The first part of our study aims to determine the quasi-stabilized states of the catalyst under different conditions, whereas the second explores dynamic changes in the structure and accompanying mass/charge-transfer processes. To decouple the catalytic and corrosion processes, experiments were undertaken under two sets of conditions: first, in the metal-precursor-free solutions to enable detectable corrosion, and second, in solutions with added Co^{2+} to suppress corrosion and enable stable catalytic operation. The latter conditions still provide essentially 100% faradaic efficiency for the OER¹⁶ and were used for the purposes of the mechanistic understanding only, whereas PEMWE equipped with the $[\text{Co-Fe-Pb}]_x\text{O}_x$ catalyst operates using pure water feed with no intentionally added Co^{2+} (Supplementary Fig. 13).

Electronic state of cobalt under steady-state conditions

First, XAS measurements were undertaken in situ under steady-state potentiostatic conditions (Fig. 1). When using a non-functionalized CFP electrode and $0.1\text{ M H}_2\text{SO}_4$ containing 5 mM Co^{2+} , a clear Co K-edge response from the dissolved species was detected, but no response to the potential was observed until reaching 2.0 V vs reversible hydrogen electrode (RHE; Fig. 1a,d). This is more positive than the Co^{2+} oxidation processes detected by FTacv (Supplementary Fig. 3c) but agrees with the onset of the OER (Supplementary Fig. 3a) and formation of minor, yet detectable by eQCM, deposit (Supplementary Fig. 9c). Even at 2.2 V vs RHE, the formal Co oxidation state detected with the initially unmodified CFP electrode remained below $3+$, indicating a notable contribution from dissolved Co^{2+} to the X-ray absorption near edge structure (XANES) data.

When analysing $[\text{Co-Fe-Pb}]_x\text{O}_x$ in the presence of 5 mM Co^{2+} , a close-to-linear dependence of the XANES rising edge energy vs the applied potential was observed (Fig. 1b,d). The Co K-edge position continuously shifts closer towards the $\text{Co}^{\text{III}}\text{OOH}$ reference and is always higher than those recorded for the bare CFP electrodes under the same conditions. In the absence of the intentionally added Co^{2+} , the in situ Co K-edge spectra of $[\text{Co-Fe-Pb}]_x\text{O}_x$ exhibit the highest energy positions of the rising edges, which increase most upon switching from open circuit to 1.8 V vs RHE (Fig. 1c,d). Application of potentials more positive than 1.9 V vs RHE does not change the spectra suggesting that the catalytically relevant quasi-steady state has been achieved. These observations indicate that the spectra obtained for $[\text{Co-Fe-Pb}]_x\text{O}_x + 5\text{ mM Co}^{2+}$ present a combination of the responses of the solid catalyst and dissolved Co^{2+} , which is supported by fitting the derivatives of the XANES data collected at 1.9 V vs RHE for three different conditions (Supplementary Fig. 18). Thus, the catalytically active state of cobalt within $[\text{Co-Fe-Pb}]_x\text{O}_x$ is independent of the presence of dissolved precursor and is therefore not directly affected by corrosion/redeposition of the catalytic sites.

The trends observed in the Co K-edge XANES were mirrored in the EXAFS data showing the combination of dissolved Co^{2+} and $[\text{Co-Fe-Pb}]_x\text{O}_x$ when analysis was undertaken in the presence of intentionally added Co^{2+} (Supplementary Fig. 19). The FT EXAFS also demonstrates that the signal at about 1.5 Å , corresponding to the first Co–O coordination sphere, remains the major structural feature of the material with no systematically observable long-range order produced in situ (Fig. 1f). This contrasts the data reported for cobalt-based OER catalysts operating in neutral-buffered electrolytes, where clear Co–Co interactions are apparent in FT EXAFS at $>2\text{ Å}$ (refs. 21,22,32,33). Specifically, the peak at about 2.8 Å was frequently reported and attributed to the cobalt- μ -(hydr)oxo-bridged species. The lack of such signal for $[\text{Co-Fe-Pb}]_x\text{O}_x$ at low pH indicates a strongly suppressed capability for cobalt (hydr)oxo-bridged species to form and/or remain stable within acidic electrolytes and highlights the structurally different nature of

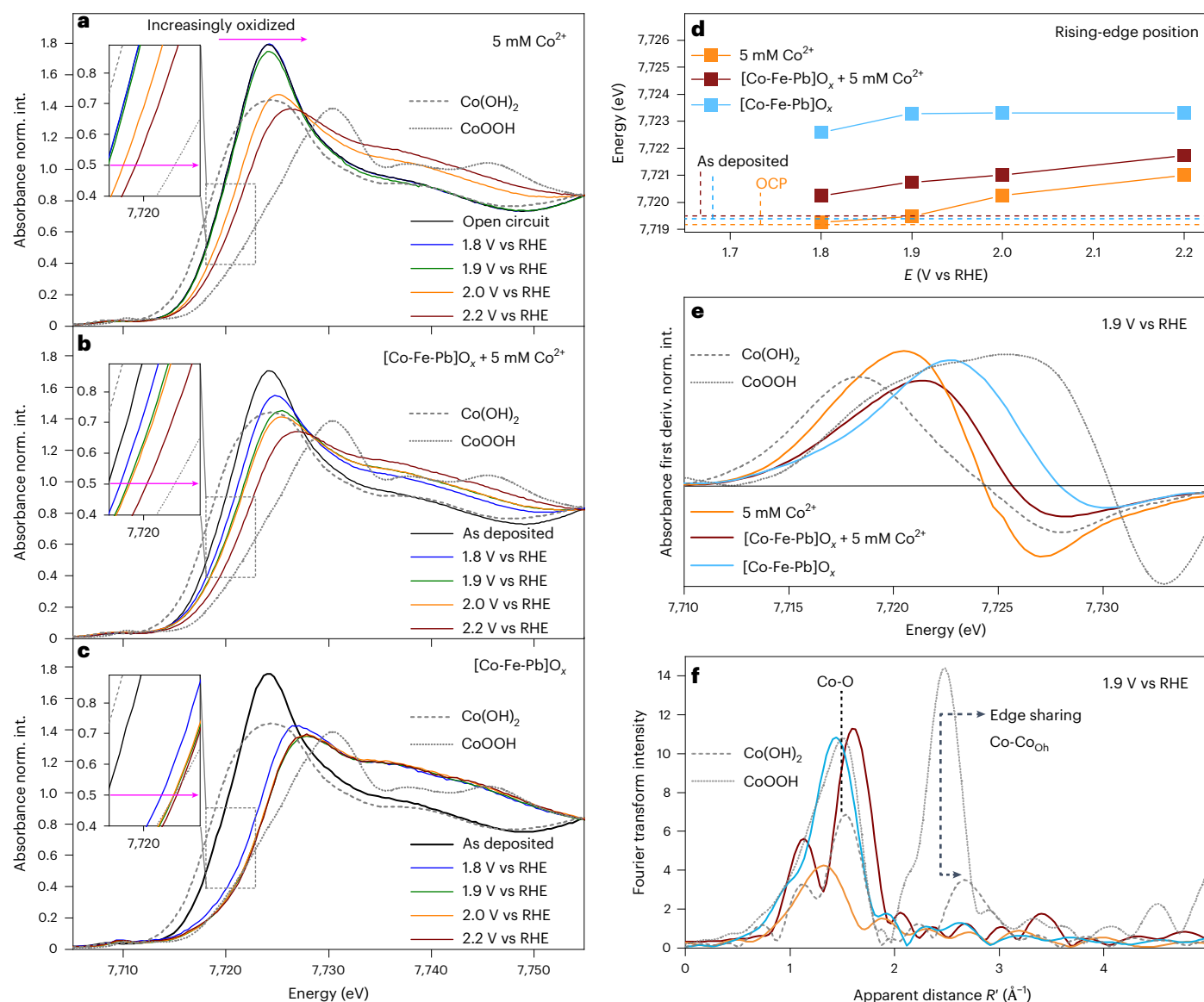


Fig. 1 | In situ Co K-edge XAS analysis of [Co-Fe-Pb]O_x. **a–c**, XANES data collected for unmodified CFP (**a**) and [Co-Fe-Pb]O_x-functionalized CFP (**b,c**) in flowed (1 ml min⁻¹) 0.1 M H₂SO₄ + 5 mM Co²⁺ (**a,b**) and nominally pure 0.1 M H₂SO₄ (**c**); black curves show data collected in situ at an open circuit (**a**) or ex situ for as-deposited catalysts (**b,c**), whereas coloured curves show in situ spectra at 1.8 (blue), 1.9 (green), 2.0 (orange) and 2.2 V vs RHE (wine). **d–f**, Rising edge position (**d**) (at 0.5 normalized intensity; norm. int.)²² vs potential (*E*) (horizontal 'OCP' and 'as-deposited' dashed lines correspond

to data recorded at open circuit within electrolyte solution and nominally dry samples before analysis, respectively), first derivative (deriv.) of the in situ XANES data collected at 1.9 V vs RHE (**e**) and FT EXAFS data (**f**) for [Co-Fe-Pb]O_x in nominally metal-free solution (sky blue), [Co-Fe-Pb]O_x with 5 mM Co²⁺ (wine) and bare CFP with 5 mM Co²⁺ (orange) at 1.9 V vs RHE. [Co-Fe-Pb]O_x was deposited by 1 h galvanostatic (10 mA cm⁻²_{geom.}) oxidation of quiescent 0.1 M H₂SO₄ containing 5 mM Co²⁺, 1 mM Fe³⁺ and 0.5 mM Pb²⁺ at 23 ± 1 °C. Data for Co(OH)₂ (dashed grey) and CoOOH (dotted grey) references are shown for comparison.

the catalytically active sites to those established for the near-neutral/alkaline conditions.

In contrast to the hard XAS, dissolved cobalt species were not detectable at the Co L_{2,3}-edges (Supplementary Fig. 20), due to differences in the X-ray attenuation lengths and therefore the depth of the analysis, in other words millimetres vs (sub)-micrometres for hard vs soft X-rays, respectively. Even when applying potentials of up to 2.1 V vs RHE, no Co L_{2,3}-edge signals were detected with a bare electrode in contact with Co²⁺ solutions. Thus, any electrodeposited cobalt(IV)-based or other CoO_x species were formed in low amounts (Supplementary Fig. 20b), consistent with the eQCM (Supplementary Fig. 9) and FTacv (Supplementary Fig. 6) data.

Well-defined Co L₃-edges spectra detected in situ for the [Co-Fe-Pb]O_x-modified electrodes at open circuit almost perfectly coincide with that

of the Co^{III}OOH reference (Fig. 2b), although it is noted that quantitative comparisons between total fluorescence yield (TFY; in situ data) and total electron yield (TEY; references) spectra should be made with caution. Application of increasingly positive potentials to [Co-Fe-Pb]O_x enhanced the intensity and shifted the Co L₃-edge main feature towards higher energies (Fig. 2a,c) until saturating between 1.9–2.0 V vs RHE (Fig. 2d,e), consistent with in situ hard XAS (Fig. 1d). These potential-induced changes were highly reproducible and reversible (Supplementary Fig. 21).

The Co L₃-edge intensity enhancement can originate from three processes: an increase in the amount of Co in the catalyst, enhanced probability of the 2p → 3d excitations due to increased density of unoccupied 3d states as cobalt is oxidized, and a decrease in covalency^{34,35}. However, only a change in the electronic structure would explain a shift

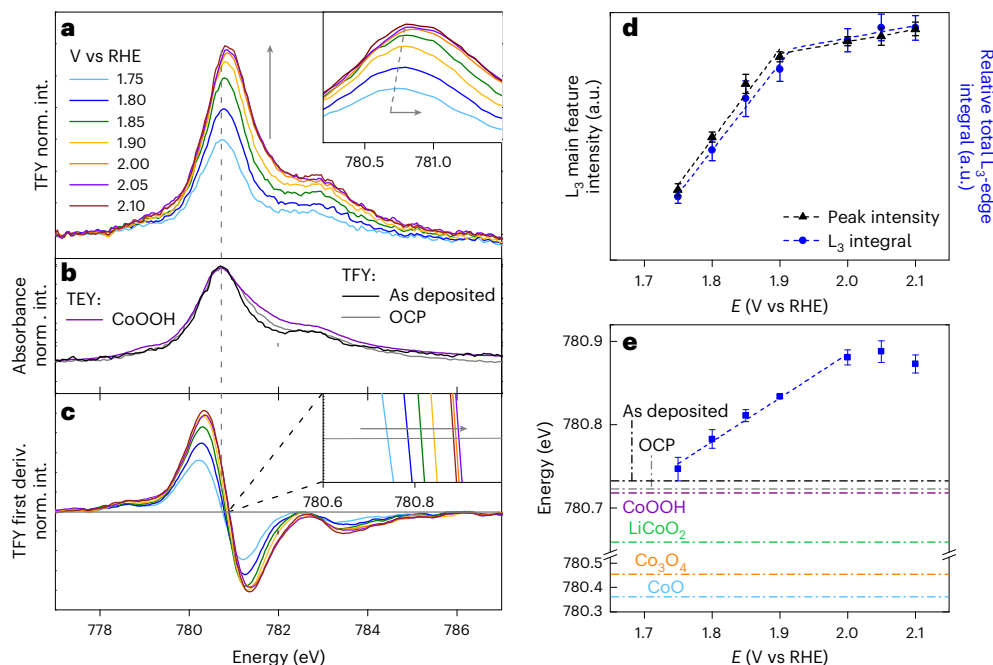


Fig. 2 | In situ Co L₃-edge XAS analysis of [Co-Fe-Pb]O_x. **a**, TFY spectra collected for the [Co-Fe-Pb]O_x-functionalized Au-Si₃N₄ membrane in flowed (10 μl min⁻¹) 0.1 M H₂SO₄ + 5 mM Co²⁺ at 1.75 (sky blue), 1.80 (blue), 1.85 (green), 1.90 (yellow), 2.00 (orange), 2.05 (violet) and 2.10 V vs RHE (wine). **b**, Ex situ TFY (grey) and in situ TFY at open circuit (black) for the as-deposited catalyst, compared to an ex situ TEY spectrum of the CoOOH reference (purple). **c**, First-order derivative of the data shown in **a** (inset shows a magnified plot of the region around derivative = 0). Arrows in **a** and **c** show changes induced by the application of progressively positive potentials; vertical dashed line in panels **a**–**c** shows position of the TFY peak maximum at 1.75 V vs RHE. **d**, **e**, Effect of potential on the Co L₃-edge main

peak intensity (black) and the integral intensity across the Co L₃-edge (blue) (**d**) and Co L₃-edge main peak position (**e**); data collected for the as-deposited catalyst ex situ, in situ at OCP, and for the reference materials are shown as horizontal dash-dotted lines in **e** (see labels in the figure). Symbols in **d** and **e** show experimental data (mean ± standard deviation from n ≥ 5 measurements; Methods), whereas dashed lines show linear fits to the data. [Co-Fe-Pb]O_x was deposited by 15 min galvanostatic (1 mA cm⁻²_{geom.}) oxidation of quiescent 0.1 M H₂SO₄ solutions containing 5 mM Co²⁺, 1 mM Fe³⁺ and 0.5 mM Pb²⁺ at 23 ± 1 °C.

in the peak position³⁴. Specifically, the shift to higher energy is consistent with stronger bonding, such as that caused by oxidation. Indeed, ligand field XAS simulations demonstrate that the experimentally detected evolution of the Co L₃-edge is consistent with partial conversion of Co³⁺ to Co⁴⁺, that is, formation of Co^{(3+δ)+} (Supplementary Note 4 and Supplementary Fig. 22). Another potential-induced change to the Co L₃-edge spectra was an increase in the width of the main feature, majorly due to a shift of the higher-energy falling edge, at potentials above about 1.9 V vs RHE (Supplementary Fig. 23). This is again consistent with an increase in the Co⁴⁺ character, as demonstrated previously for delithiated Li_{1-x}CoO₂ (ref. 36). Additionally, the Co L₃-edge broadening might be associated with the contributions of surface species involved in the OER catalysis and therefore developing at progressively positive potentials. First principles simulations suggest a change in the catalytic surface state inducing a notable positive energy shift of simulated XAS at about 1.9 V vs computational hydrogen electrode (Supplementary Note 5 and Supplementary Figs. 24–28). Because our in situ Co L₃-edge data might have a significant contribution from the bulk cobalt states, the contribution of this surface change is probably not substantial and only causing slight broadening rather than pronounced spectral changes.

Thus, both Co K- and L₃-edge spectroelectrochemical data, supported by theoretical analysis, collectively indicate formation of the Co^{(3+δ)+} active sites during the OER at low pH, which are structurally different from the active sites of the cobalt-based catalysts operating in near-neutral and alkaline electrolytes.

Potentiodynamic evolution of the catalyst

Further, we focused on the evolution of the catalyst under dynamic conditions using electrochemical, gravimetric and spectroscopic

techniques to probe the dynamics of key processes within the cobalt active sites during the OER. FTacv was used to correlate the catalytic current and key charge-transfer process(es) that underpin it^{37–40}, whereas the corresponding gravimetric and redox changes were investigated by eQCM^{29,41} and fixed energy X-ray absorption voltammetry (FEXRAV)^{42–44}.

To explore the potential-dependent trends of the charge-transfer process directly coupled to the OER catalysed by cobalt sites (Supplementary Note 1 provides extended explanation), a series of electrodes with varied [Co-Fe-Pb]O_x loading was analysed both in the presence and absence of 5 mM Co²⁺ (Fig. 3, Supplementary Note 6 and Supplementary Figs. 29 and 30). a.c. harmonic components exhibited well-defined signals of the OER-coupled charge transfer (Fig. 3b,d), the position of which on the potential scale correlated with the catalytic direct current (d.c.) (Fig. 3e). This mimics, in a qualitative way, the behaviour for the OER in borate buffer catalysed by CoO_x (and MnO_x and NiO_x)^{30,37} and indicates that the mechanism of the reaction might be described by conceptually similar electrokinetic models, though clearly with distinct parameters and facilitated by different active sites, at different pH.

The only distinction between the voltammetric data obtained with and without intentionally added Co²⁺ was in the OER activity, which was lower in the latter case due to suppressed redeposition of cobalt oxide species and therefore lower number of active sites (Fig. 3a,c). This was mirrored in shifts of the OER-coupled charge transfer towards more positive potentials (Fig. 3b,d). Most importantly, the dependences of the OER direct current on the position of the a.c. harmonic OER-coupled signal with and without 5 mM Co²⁺ closely overlapped (Fig. 3e). This demonstrates that the electrokinetic parameters of the OER do not depend on the presence of the intentionally added Co²⁺, that is, the mechanism of the process does not change upon intensification of the active site corrosion or regeneration.

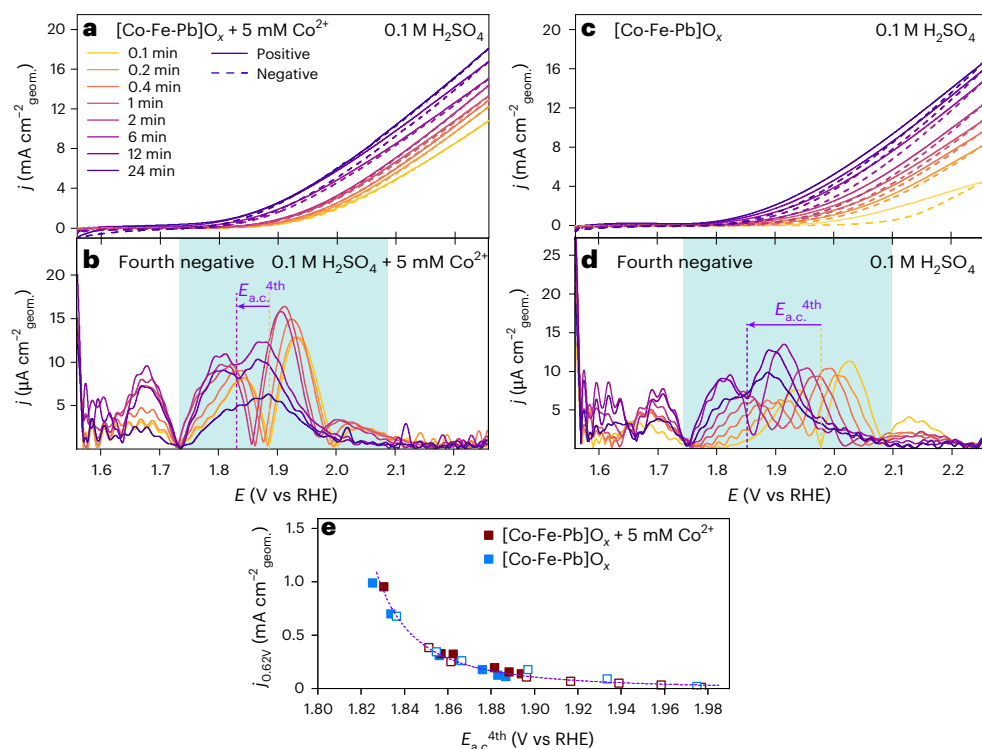


Fig. 3 | Potential dependence of the OER-coupled charge transfer in [Co-Fe-Pb]O_x. **a–d**, FTac voltammetric ($f = 9.02$ Hz, $\Delta E = 0.080$ V; first scans; 23 ± 1 °C) data collected for the catalyst at different loadings on an FTO electrode in quiescent 0.1 M H₂SO₄ in the presence (**a,b**) and in the absence (**c,d**) of intentionally added 5 mM Co²⁺, shown as aperiodic d.c. (**a,c**) and fourth a.c. harmonic components (**b,d**) (complete datasets are provided in Supplementary Figs. 29 and 30); arrows in **b** and **d** show shifts of the OER-coupled signal, highlighted with blue background, induced by increase in the catalyst loading. **e**, Dependence of the OER direct current density at 1.85 V vs RHE ($\eta \approx 0.62$ V) in

the reverse (filled squares) and positive sweeps (empty squares) on the position of the OER-coupled charge-transfer process in fourth a.c. harmonics derived from **a–d** and Supplementary Figs. 29 and 30 for the data with (wine) and without (sky blue) added 5 mM Co²⁺; dashed line is guide to the eye. The catalyst loading was varied by changing the electrodeposition time (0.1, 0.2, 0.4, 1, 2, 6, 12 and 24 min) and is colour-coded as shown in **a**. Depositions were undertaken in quiescent 0.1 M H₂SO₄ electrolytes containing 5 mM Co, 1 mM Fe and 0.5 mM Pb²⁺ at 23 ± 1 °C.

Another important effect of added Co²⁺ was a low intensity (hence with slow charge-transfer kinetics) yet identifiable process at about 1.70–1.75 V vs RHE (Supplementary Fig. 29g), which was much weaker for nominally pure 0.1 M H₂SO₄ (Supplementary Fig. 30g). FTacv analysis suggests that this process is associated with the oxidation of Co²⁺, possibly producing passivating Co⁴⁺-based species (Supplementary Note 1). The fact that it was also detected, yet at much lower intensity, without intentionally added Co²⁺ is due to partial dissolution of cobalt into the solution, as occurs in the case of all Co-based OER catalysts operating at low pH. Importantly, the putative Co^{2+/4+} process is clearly not coupled to the OER as its position does not change with the activity³⁷.

The FTacv analysis suggests qualitative similarity in the overarching kinetic principles of the cobalt-catalysed OER at different pH and indicates that the major role of the intentionally added Co²⁺ precursor is to preserve the active sites rather than alter the kinetics of the process. Apart from reformation of the original active sites by electrodeposition, this preservation might be facilitated by the formation of passivating, corrosion-resistant Co⁴⁺-based species, through oxidation of dissolved Co²⁺. Because no explicit indications of additional phases were found by XAS (*vide supra*), these species might only be present in very small amounts on the catalyst surface only, which however, would be sufficient to stabilize the active sites^{7,8,10,12}.

FEXRAV data are obtained by measuring X-ray absorption at a fixed energy while the electrode is subjected to voltammetric cycling. The data from such experiments can be presented as plots of the TFY vs potential along with corresponding voltammograms to enable direct correlations between the electrochemical data and changes in the

states of the element probed (Fig. 4 and Supplementary Figs. 31–34)⁴⁴. Here, Co K-edge FEXRAV data were recorded at five different energies to probe potential-dependent responses from the background fluorescent signal before the edge (7,700 eV), cobalt 1s → 3d transitions (7,710 eV), apparent cobalt oxidation state (7,720 and 7,725 eV) and the raw fluorescence signal after the edge (8,000 eV) (Supplementary Figs. 31 and 32). Because X-ray absorbance at all energies probed are affected by the cobalt/sample concentration and background response, these effects need to be taken into consideration during interpretations. Major soft FEXRAV measurements were undertaken at the excitation energy of 780.75 eV, which corresponds to the maximum of the Co L₃-edge at 1.75 V vs RHE—the negative switching potential used in these experiments. Response at the second Co L₃-edge feature (782.9 eV) followed the same trends but was weaker in intensity (Supplementary Fig. 33a–c).

Co K-edge FEXRAV of the catalyst-free electrode in the presence of 5 mM Co²⁺ revealed only a weak response at 7,720 and 7,725 eV with no correlations against the potential (Supplementary Figs. 31d–f and 32f–j). Given the observation of clear potential-dependent changes in the steady-state Co K-edge XAS under the same conditions (Fig. 1a and Supplementary Fig. 19b,e), we conclude that the electrooxidation of dissolved Co²⁺ on a catalyst-free surface is a slow process, consistent with FTacv (Supplementary Note 1 and discussions above) and cannot be resolved by FEXRAV at a potential sweep rate of 0.005 V s⁻¹. At the same time, well-defined potentiodynamic Co K-edge responses were detected for [Co-Fe-Pb]O_x (Fig. 4d,e and Supplementary Figs. 31a–c,g–i and 32a–e,k–o). In the presence of 5 mM Co²⁺, the FEXRAV intensity at 8,000 eV increased/decreased at more/less positive potentials

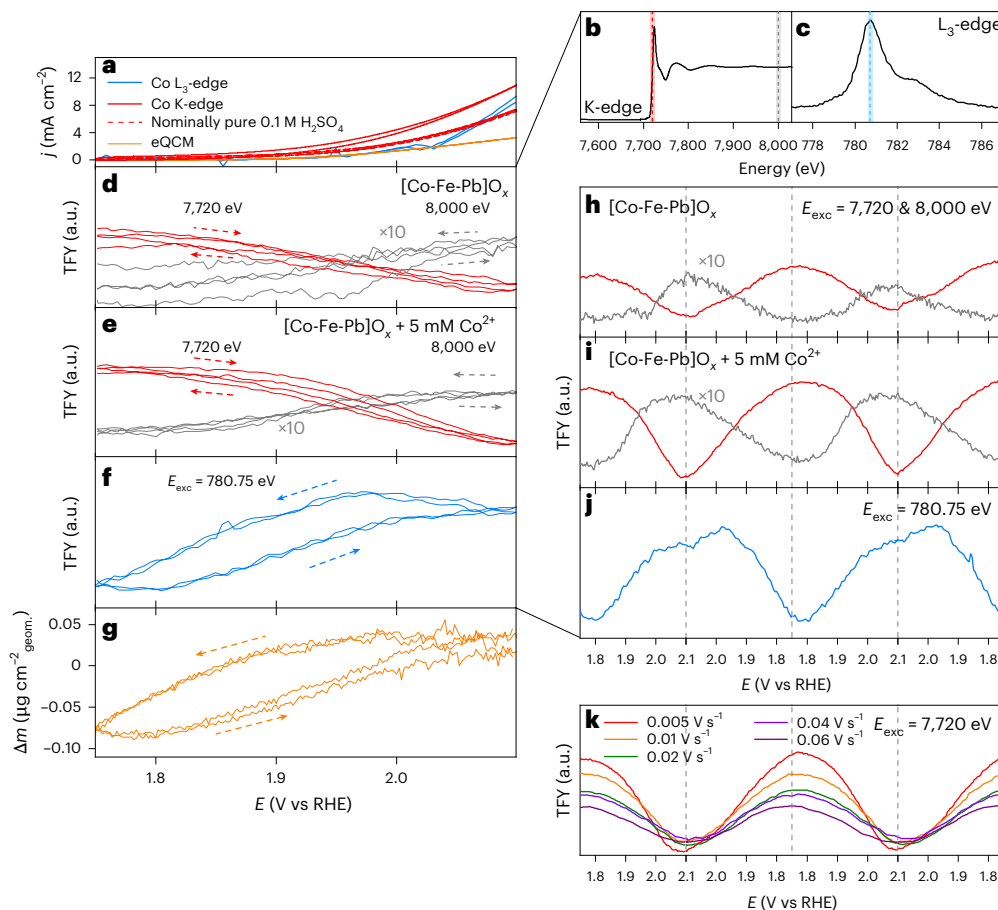


Fig. 4 | Potentiodynamic in situ XAS and eQCM analysis of [Co-Fe-Pb] O_x .

a, Cyclic voltammograms ($\nu = 0.005 \text{ V s}^{-1}$) recorded during the hard XAS (solid red and dashed red), soft XAS (sky blue) and eQCM (orange) experiments in flowed (1 ml min^{-1} for Co K-edge and eQCM, $10 \mu\text{l min}^{-1}$ for Co $\text{L}_{3\text{-edge}}$) $0.1 \text{ M H}_2\text{SO}_4$ (dashed) and $0.1 \text{ M H}_2\text{SO}_4 + 5 \text{ mM Co}^{2+}$ (solid). **b, c**, Positions of energies used for FEXRAV on typical Co K- (**b**) and $\text{L}_{3\text{-edge}}$ spectra (**c**). **d–k**, Corresponding potentiodynamic ($\nu = 0.005 \text{ V s}^{-1}$) evolution of the TFY signals at 7,720 (red) and 8,000 eV (grey; multiplied by a factor of 10) (**d, e, h, i**) in $0.1 \text{ M H}_2\text{SO}_4$ (**d, h**) and

$0.1 \text{ M H}_2\text{SO}_4 + 5 \text{ mM Co}^{2+}$ (**e, i**), TFY signal at 780.75 eV (**f, j**), and mass change (**g**); arrows show the sweep direction. **k**, Effect of the scan rate (values in the figure) on the potentiodynamic evolution of the TFY signal at 7,720 eV in $0.1 \text{ M H}_2\text{SO}_4 + 5 \text{ mM Co}^{2+}$. **h–k** show time-resolved data on a potential scale with vertical dashed lines showing the potential switching points. [Co-Fe-Pb] O_x was deposited onto CFP (Co K-edge), Au- Si_3N_4 membrane (Co $\text{L}_{3\text{-edge}}$) and Au-coated quartz crystal (eQCM) by galvanostatic oxidation at 10 and 5 mA cm^{-2} , respectively, of quiescent $0.1 \text{ M H}_2\text{SO}_4 + 5 \text{ mM Co}^{2+}$, 1 mM Fe^{3+} and 0.5 mM Pb^{2+} at $23 \pm 1^\circ\text{C}$.

(Fig. 4e, i), which is consistent with the eQCM data (Fig. 4g) and demonstrates the dynamic corrosion/reformation of the cobalt active sites. The absorbance at 7,710, 7,720 and 7,725 eV followed an inverse trend, indicating that the response at the (pre)edge is dominated by the electrochemically induced electronic changes rather than the amount of detectable cobalt, both in the presence and absence of intentionally added Co^{2+} (Fig. 4d, e, h, i and Supplementary Figs. 31a–c, g–i and 32a–e, k–o).

The amplitude of the Co K-edge FEXRAV data collected for [Co-Fe-Pb] O_x without intentionally added Co^{2+} was lower as compared to experiments with 5 mM Co^{2+} (Fig. 4d, h and Supplementary Figs. 31g–i and 32k–o). The overall lower intensity at 7,720 and 7,725 eV reflects the higher oxidation state of cobalt, although one cannot exclude a small but measurable effect of the decrease in the amount of Co active sites, which is seen from both electrocatalytic (Fig. 4a) and FEXRAV data at 8,000 eV (Fig. 4d, e, h, i). However, this effect cannot explain the lack of pronounced changes at the Co K pre-edge at 7,710 eV, which are clearly detected for the [Co-Fe-Pb] $\text{O}_x + 5 \text{ mM Co}^{2+}$ combination only. Whereas one might ascribe this signal to the processes involving incorporation of cobalt into the solid catalyst matrix through electrooxidation of dissolved Co^{2+} (given that no response is detected for the catalyst-free electrode; Supplementary Fig. 31f), we acknowledge that an unambiguous explanation of this phenomenon is yet to be established. Overall, the

observations summarized above indicate that the Co K-edge FEXRAV data represent contributions from the cobalt species both within the solution and [Co-Fe-Pb] O_x .

The FEXRAV response at 780.75 eV ($\text{L}_{3\text{-edge}}$) was also highly reversible (Fig. 4f), but the shape of the signals was different to that detected at 7,720 eV (K-edge). In the latter case, the change of the intensity was continuous and reverted with minimal delay upon switching the direction of the potential sweep (Fig. 4h, i). In contrast, the $\text{L}_{3\text{-edge}}$ intensity was rapidly rising until about 1.95 V vs RHE, followed by a slower increase, which did not cease even upon switching the direction of the potential sweep to a negative direction (Fig. 4j). Only after reaching about 2 V vs RHE in the negative sweep, the 780.75 eV TFY signal decreased in intensity following a close-to-linear dependence on the potential. The difference in the FEXRAV between the two edges might arise from the lack of interference from the dissolved Co species at the Co $\text{L}_{3\text{-edge}}$ (Supplementary Fig. 20), that is, response in this case is pertinent to the [Co-Fe-Pb] O_x active sites only. The Co $\text{L}_{3\text{-edge}}$ FEXRAV data reveal that two processes with different charge-transfer kinetics contribute to changes in the electronic state of cobalt during the OER at low pH. First is most likely the oxidation of cobalt producing $\text{Co}^{(3+5)+}$ active sites (Supplementary Fig. 22), whereas the second might be associated with the evolution of the catalytic surface states (Supplementary Fig. 28).

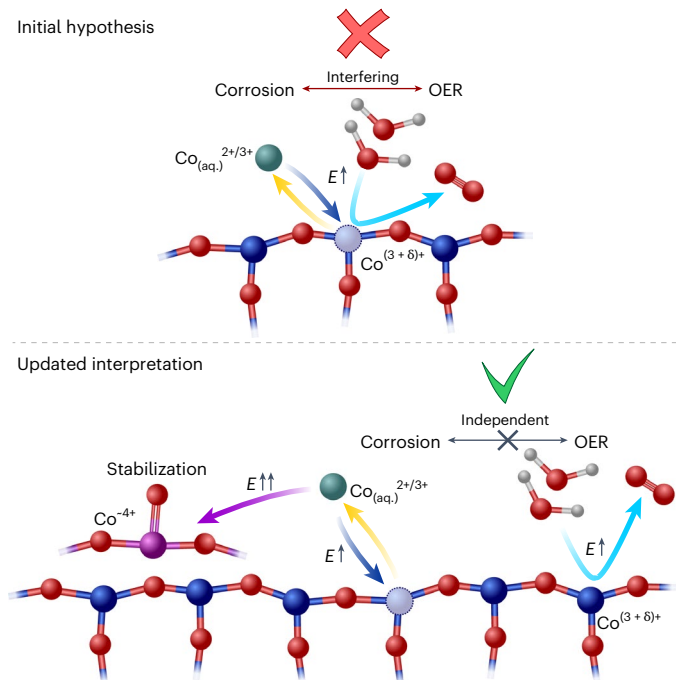


Fig. 5 | Interfering vs independent OER and cobalt corrosion. Initial hypothesis is based on a common observation of corrosion of the OER catalysts in operation due to electrooxidation. Note that the schemes are purely illustrative and do not aim to represent the exact structures of the cobalt-based species within an OER catalyst. Arrows show: the OER (light blue), corrosion of the active sites (yellow), electrooxidative regeneration of the active sites (blue) and formation of the low-activity but high-stability cobalt(IV)-based species (purple).

FEXRAV experiments at the O K-edge revealed a clear correlation between the OER catalytic current and absorption at 531.2 eV (Supplementary Figs. 33d–f and 34f). The latter signal is ascribed to the $O\ 1s \rightarrow 2p\ O(\pi^*)$ transition of O_2 gas (Supplementary Fig. 35), indicating the direct observation of the reaction product. Further, comparisons of potentiostatic O K-edge spectra taken at 2.05 and 1.75 V vs RHE suggest the emergence of minor features at about 527.5 and 529.0 eV (Supplementary Fig. 36), which provides an additional indication for the formation of the $Co^{(3+\delta)+}$ species⁴⁵.

Finalizing the FEXRAV analysis, the effect of the scan rate on the Co K-edge XAS response was investigated for $[Co-Fe-Pb]O_x$ (Fig. 4k and Supplementary Fig. 37). Relative changes in the TFY signal at 7,720 eV during the Co K-edge FEXRAV analysis at 0.005 V s⁻¹ and during steady-state in situ XAS were similar, indicating that the potentiodynamic mode at a slow scan rate provided close-to-complete change in the cobalt oxidation states when dissolved Co^{2+} was present (Supplementary Fig. 38a). However, increasing the scan rate even to 0.010 V s⁻¹ under these conditions produced a pronounced dampening effect on the intensity of the FEXRAV signal at 7,720 eV, where redox changes dominate the Co K-edge spectral features (Fig. 4k). Moreover, comparing relative changes in TFY at 7,720 eV measured by FEXRAV at 0.005 V s⁻¹, and steady-state analysis in the absence of intentionally added Co^{2+} indicated a lower degree of oxidation achieved at this low potential scan rate (Supplementary Fig. 38b). These observations indicate that the effective timescale of the transformation of dissolved Co^{2+} is comparable to the timescale of the voltammetric experiment at 0.005 V s⁻¹, whereas the dynamics of the cobalt-based charge transfer within $[Co-Fe-Pb]O_x$ is even slower. Overall, our data demonstrate that stabilization of the active state of the catalyst during the OER at low pH, which includes the interplay of corrosion and oxidation of cobalt species, occurs on a timescale of minutes (Fig. 4k). This relatively slow dynamics needs to be considered

in both fundamental studies as well as practical applications of the cobalt-based low-pH OER catalysts.

Discussion

The multi-technique study presented here uncovers the potential-dependant events that dictate both the mass and redox changes occurring within cobalt active sites during the OER at low pH. The key insights were derived from correlations of the data provided by all methods employed, highlighting the effectiveness of using a comprehensive suite of electrochemical, gravimetric and spectroscopic techniques when investigating complicated electrocatalytic processes, such as acidic OER catalysed by non-noble catalysts that are prone to corrosion.

Our data suggest a previously unknown contribution of low-activity Co^{4+} -based oxide species into stabilization of the cobalt-based low-pH catalysts, in addition to the electrooxidation of dissolved Co^{2+} into high-activity cobalt oxo-sites. While these processes support fast kinetics of the OER-coupled charge transfer through stabilization of the active sites, they do not affect their intrinsic catalytic activity. In other words, corrosion and redeposition processes are not directly coupled to the catalytic process but occur in parallel (Fig. 5).

The time-resolved measurements indicate that the evolution of the catalyst to achieve the active stabilized state is not a fast process, occurring on a timescale of minutes. The catalytically active cobalt sites during the acidic OER adopt an oxidation state higher than 3+ and lack long-range order, that is, are structurally different from the cobalt- μ -(hydr)oxo states reported for the near-neutral and alkaline conditions. This understanding can guide the development of strategies for the design of practical and affordable cobalt-based anode catalysts for proton-exchange water electrolyzers as needed to enable the use of these highly-effective devices for the sustainable hydrogen production on a multi-gigawatt scale.

Methods

Materials

Metal-precursor solutions were prepared using reagent grade chemicals: $Co(NO_3)_2 \cdot 6H_2O$ (>98%, Sigma), $Fe(NO_3)_3 \cdot 9H_2O$ (>98%, Sigma), $Pb(NO_3)_2 \cdot 6H_2O$ (>99.5%, Merck), H_2SO_4 (95–97%, Sigma). Other reagents used were H_2O_2 (30%, Merck), HNO_3 (70%, Ajax FineChem), HCl (36%, Ajax FineChem), H_2PtCl_6 (99.9%, Sigma) and *iso*-propanol (>99, CSA Scientific). Deionized water (Sartorius Arium Comfort I Ultrapure water system H2O-I-1-UV-T; resistivity 18.2 MΩ cm at 23 °C) was used in all experiments other than the soft XAS and eQCM studies where ROTISOLV HPLC Gradient Grade deionized water (18.2 MΩ cm at 23 °C) was used.

The proton-exchange membrane water electrolysis (PEMWE) cell utilized Grade 1 Titanium flat current collectors (Specialty Metals). Porous transport layers were constructed following a gradient mesh approach⁴⁶ using three Ti mesh layers (Unique Wire Weaving Co.) stacked in the order of descending size and porosity arrangement from the Ti current collectors in both anode and cathode compartments (layer in contact with the anode/cathode—0.23-mm wire diameter; 21.2% open area; middle layer—0.61-mm wire diameter; 35% open area; layer contacting current collector—0.77-mm wire diameter; 51% open area). A 200-μm thick PtTi-felt with a 30-nm Pt coating (Tanaka) was used as an anode substrate. A 190-μm thick hydrophobic carbon fibre paper (Toray Carbon Paper TGP-H-060) was used as a cathode substrate. 20 wt% Pt on Vulcan XC-72 (57080081, Fuel Cell Store) was used as a cathode catalyst. 5 wt% PFSA ionomer dispersion (28020001, Fuel Cell Store) was used for the cathode catalyst ink preparation.

Working electrode substrates

Fluorine-doped tin(IV) oxide coated glass (FTO) slides (TEC8; 10 cm × 10 cm, sheet resistance 8 Ω sq⁻¹) were purchased from Dyesol Ltd. and used to prepare electrodes following published procedures^{16,39}.

The slides were cleaned by ultrasonication (Elmasonic S300H bath, 1,500 W) in 2 wt% Helmanex_(aq.), water and ethanol for 20 min in each media, dried under N₂ flow and plasma treated at 1,000 mTorr for 5 min (Harrick plasma cleaner). An active area of 2 mm × 2 mm (0.04 cm²) was defined by laser engraving (Universal Laser Systems, VLS350) and polyimide Kapton tape. Before applying the tape, FTO electrodes were treated with fresh Caro's acid for 10 s and washed with water. Spectra-Carb carbon fibre paper electrodes (Fuel Cell Store) were pre-treated with HNO₃(conc.) for 12–16 h, rinsed with water, dried under N₂ flow and laminated into PET, leaving a circular area (Ø8 mm, 0.50 cm²) defined by laser engraving exposed³⁹. Gold-coated silicon nitride (Au-Si₃N₄) X-ray permeable membranes (1.0 mm × 0.5 mm × 75 nm) etched into a Si support frame (10.0 mm × 10.0 mm × 381 µm) and covered with 20 nm Au on a 5 nm Ti adhesion layer (Silson Ltd.) producing an electrochemically active area of 0.04 cm² (ref. 47), were used as electrodes for soft XAS⁴⁸. 5 MHz eQCM discs coated with 5-nm Ti and 100-nm Au layers (Quarztechnik GmbH) with a surface area of 1 cm² were used for eQCM. The discs were sonicated in an ethanol:2-propanol (1:1 vol) mixture for 10 min and rinsed with deionized water and 0.1 M H₂SO₄ before measurements.

Electrochemical equipment

FTacv, eQCM and in situ XAS experiments, and preparation of the samples for SEM/EDS and XPS analysis, were undertaken at ambient temperature (23 ± 1 °C). FTacv was performed using a custom-made instrument³⁰. In situ Co K-edge and soft XAS experiments were undertaken using a Bio-Logic VSP electrochemical workstation, whereas eQCM studies were performed using an Interface 1010E potentiostat. The PEMWE experiments used a Bio-Logic SP-50e and a BSTR-10A high current booster channel. The FTacv measurements were undertaken in a two-compartment cell with the working and auxiliary electrode chambers separated by a low-porosity P4 glass frit. The same type of cell was used for the [Co-Fe-Pb]O_x electrodeposition for the FTacv, in situ XAS or eQCM analysis. eQCM measurements were undertaken using a Gamry Instruments eQCM 10 M cell. In situ XAS studies used specialized cells described below. Potentials were measured against either Ag|AgCl|KCl_(sat.) (CHI) (FTacv, eQCM) or a 'leak-free' Ag|AgCl|KCl(3.4 M) LF-1-100 reference electrode purchased from Innovative Instruments (XAS). Potentials of Ag|AgCl|KCl_(sat.) was calibrated against a reversible hydrogen electrode (RHE) following the reported procedures³⁹, before and after experiments to ensure the stability of the reference electrodes. The 'leak-free' Ag|AgCl|KCl(3.4 M) LF-1-100-type reference electrodes were monitored for any potential shifts against a Ag|AgCl|KCl_(sat.) master reference electrode that was calibrated against the RHE. The reference electrode was confined within a fritted (P4) glass tube positioned at a fixed short distance from the centre of the working electrode. High surface area platinum mesh, platinum wire or platinized titanium grid (Fuel Cell Store) were used as the auxiliary electrodes. Before measurements, Pt was cleaned using a flame torch, while platinized titanium was cleaned by soaking in H₂SO₄ (conc.): H₂O₂ (30 wt%) (1:1 vol.) for several minutes.

Before measurements, all glassware used for electrodepositions were cleaned by soaking in a freshly prepared HNO₃ (conc.): HCl (1:3 vol.) mixture for at least 12 h and then rinsed with copious amounts of water to exclude any cross-contamination.

Electrochemical measurements

Before galvanostatic [Co-Fe-Pb]O_x electrodeposition, five cyclic voltammograms ($\nu = 0.020 \text{ V s}^{-1}$) within the potential range of 0.2–1.4 V vs Ag|AgCl|KCl_(sat.) in 0.1 M H₂SO₄ were recorded to ensure the electrode surface was clean and measurements were consistent. Further, the electrode was put in contact with the [Co-Fe-Pb]O_x precursor solution and cyclic voltammograms ($\nu = 0.020 \text{ V s}^{-1}$) between 1.0 and 2.0 V vs Ag|AgCl|KCl_(sat.) were recorded before galvanostatic deposition at a required current density (10 mA cm⁻² for Co K-edge XAS and FTacv, 1 mA cm⁻² for soft XAS, 5 mA cm⁻² for eQCM).

FTacv measurements used an amplitude of $\Delta E = 0.080 \text{ V}$, frequency of 9.02 Hz and scan rates defined by the potential range. Data were collected as two consecutive voltammetric cycles; second cycles were used for analysis.

Catalyst functionalization onto electrode substrates

Precursor solutions were prepared via two highly order-sensitive procedures. For hard XAS, XPS and FTacv, 2 ml of 50 mM Co(NO₃)₂ and then 2 ml of 10 mM Fe(NO₃)₃ in 1 M H₂SO₄ were mixed with 15 ml of H₂O; then 1 ml of 10 mM Pb(NO₃)₂ was carefully pipetted drop-wise. For the Co L₃-edge and eQCM, 2 ml of 50 mM Co(NO₃)₂ and then 1 ml of 10 mM Pb(NO₃)₂ were mixed with 15 ml of H₂O; then 2 ml of Fe(NO₃)₃ in 1 M H₂SO₄ was carefully pipetted drop-wise. The last steps in both procedures must be undertaken slowly and with high care to avoid excessive agitation, which induces precipitation of PbSO₄. The latter was meticulously avoided to ensure reproducibility of the results. Precursor solutions were prepared immediately before electrodeposition of [Co-Fe-Pb]O_x.

For the PEMWE test, a [Co-Fe-Pb]O_x/PtTi anode was fabricated by a 120-min galvanostatic electrodeposition (50 mA cm⁻²_{geom.}) using a 0.5 M HNO₃ solution containing 100 mM Co(NO₃)₂, 20 mM Fe(NO₃)₃ and 20 mM Pb(NO₃)₂ at 23 ± 1 °C. To fabricate the cathode, the Aquivion E98-09S membrane was coated with the 20 wt% Pt/C catalyst to achieve a loading of about 0.8 mg_{Pt} cm⁻²_{geom.} by ultrasonic spray coating (FocusMist Ultrasonic Atomizer Nozzle, Siansonic) of a 5 mg ml⁻¹ dispersion of the catalyst in *iso*-propanol:water mixture (2.8:1 vol) containing 0.25 wt% PFSA ionomer dispersion at 110 ± 1 °C. Before use, the catalyst dispersion was ultrasonicated for 1 h (Ultrasonic power generator K 8, Meinhardt Ultrasonics). The functionalized membrane and anode were hot pressed at 18 kg cm⁻² and 135 ± 1 °C for 2 min.

Physical characterization

Scanning electron micrographs were collected with an FEI Quanta 3D FIBSEM microscope at 15 kV voltage. Electrodes were adhered to the SEM stubs using a sticky carbon tape. No additional conductive coatings were applied.

Energy-dispersive X-ray spectra were collected using a Jeol IT800 SHL instrument equipped with an Oxford Instruments Ultim Max 170 silicon drift X-ray detector. Instrumental settings were as follows: 15-kV landing voltage, 0.80-nA probe current and 10-mm working distance. Electrodes were adhered to the SEM stubs using a sticky carbon tape. No additional conductive coatings were applied to the samples.

Inductively coupled plasma mass spectrometric analysis was conducted using a Perkin Elmer NexION 2000 instrument. The 5 ml aliquots of the PEMWE water feed were diluted twofold with 2 wt% HNO₃ for analysis. Electrodes used for the measurements of the fraction of redox active cobalt were digested in 50 ml of 0.5 M HNO₃ until complete dissolution of [Co-Fe-Pb]O_x (~16 h); 2 ml of the resulting solution was diluted fivefold with 2 wt% HNO₃. Sc, Ge and Rh ions were introduced into the sample inlet as internal standards for Co and Fe and Pb isotopes, respectively. Background counts measured for the 2 wt% HNO₃ carrier solution were subtracted from the measurements. Calibration curves were constructed using standard samples obtained by dilutions of commercial stock solutions. The Co and Fe analyses were conducted with He gas, whereas the Pb was conducted with Ar gas.

X-ray photoelectron spectroscopy (XPS) data were recorded using a Nexsa Surface Analysis System (Thermo Fisher Scientific) equipped with a monochromated Al K_α source (15 kV × 12 mA) and a hemispherical analyser operating in a fixed analyser transmission mode. The total pressure in the main vacuum chamber during the analysis varied between 10⁻⁹ and 10⁻⁸ mbar. Survey spectra were recorded at a pass energy of 200 eV and a step size of 1 eV, whereas high-resolution spectra used 50 eV pass energy with 0.1 eV step size. The latter settings produced an FWHM of 0.8–0.9 eV for the Ag 3d_{5/2} reference spectrum.

All samples were rinsed with water to remove any dissolved precursor and dried under vacuum at $100 \pm 1^\circ\text{C}$ for 24 h. The dried samples were mounted on the sample stage using carbon tape. All samples were analysed in a floating mode. Binding energies were calibrated against the aliphatic C–C 1s peak, with position set to 284.8 eV.

Co K-edge X-ray absorption spectra were collected at the Australian Synchrotron using the multipole wiggler XAS beamline (12-ID) operated with an electron beam energy of 3.0 GeV and a beam current of 200 mA (top-up mode). The Co K-edge, Fe K-edge and Pb L₃-edge data were recorded using Si(111) monochromators and focusing optics⁴⁹ in fluorescence mode using a 100-element Ge detector. Analysis of the CoO, Co(OH)₂, Co₃O₄ and CoOOH references was done using pressed powder pellets containing ~1 wt% of the compound of interest diluted in boron nitride (Sigma). The spectra were referenced against the data for Co (7,709 eV), Pb (13,025 eV) and Fe foils (7,112 eV). Ex situ analysis of [Co-Fe-Pb]O_x was done using samples electrodeposited on CFP.

In situ Co K-edge XAS measurements were undertaken using a spectroelectrochemical cell equipped with a Teflon fabric reinforced Nafion N324 membrane between the working and auxiliary electrode compartments²². A peristaltic pump (Longer BT100-2J) was used to fill/empty the cell with the electrolyte solution and to maintain the electrolyte solution flow of about 1 ml min⁻¹ during analysis.

Steady-state spectra were acquired about 10 min following application of the potential to ensure the equilibration of the system. For every potentiostatic Co K-edge measurement, about 15-min long replicate scans were recorded at each sample spot for all datasets. Typically, two scans were taken on one spot and two scans were taken on a second spot to ensure no detectable contribution of beam effects for the resultant averaged spectra. This experimental protocol yielded a typical analysis time of about 90 min per potential. Raw data obtained from the beamline were converted using Sakura⁵⁰ and processed using a combination of Athena⁵¹, PySpline⁵² and MSEXcel.

Soft X-ray absorption spectroscopic studies were undertaken at the U49-2 PGM-1 beamline utilizing the LiXEdrom endstation⁵³ at the BESSY II synchrotron facility in Berlin, Germany. CoO, Co₃O₄, LiCoO₂ and CoOOH powders dispersed on conductive Cu-tape were analysed in TEY mode. Measurements were conducted using the third harmonic and the following beamline parameters: cff 5, diffraction order 2, undulator offset 0.0 and beamline slit 100 μm. The aperture was set to a symmetric opening of 2.0 mm × 2.0 mm for measurements across the Co L_{2,3}-edges and O K-edge. The TFY signal was collected by an XUV-100 silicon photodiode. Spectra were collected by scanning the incident X-ray energy across an energy range of 770 to 810 eV covering the full L_{2,3}-edge spectrum of Co and from 775 to 795 eV to cover the Co L₃-edge only. O K-edge spectra were measured across an energy range of 525 to 550 eV. Measurements were conducted in continuous scan mode, yielding data points in about 0.05 eV steps with an energy resolution of the incident beam $\Delta E \approx 0.1$ eV. Spectra were normalized to the drain current of the refocusing mirror ($I_{\text{TFY}}/I_{\text{mir}}$) to account for X-ray flux variations in top-up mode and to obtain spectra that are comparable in relative intensity. To account for contaminations on the beamline optics, the spectra were additionally normalized to the beam intensity in the experimental chamber measured with a diode in the beam path at identical beamline settings ($I_{\text{diode}}/I_{\text{mir}}$), yielding a total normalization of the TFY signal to the incident photon intensity ($I_{\text{TFY}}/I_{\text{diode}}$). The top-up mode operation of the BESSY II storage ring, in very few cases, caused glitches in the mirror current; in situations where these glitches disturbed spectral features, single clear outliers in the mirror current data were removed from the dataset.

In situ Co L₃- and O K-edge studies were performed using a vacuum compatible flow cell in the TFY mode⁴⁷. Nafion 117 membrane (183 μm, Sigma-Aldrich) was used to separate the working and auxiliary electrode compartments. The Nafion membrane was cut into circles (Ø15 mm) and soaked in 1 M H₂SO₄. The cell containing the [Co-Fe-Pb]O_x catalyst was then filled with either pure 0.1 M H₂SO₄ or containing

5 mM Co²⁺. Electrolyte was flown during the experiments using a KD Scientific Gemini 88 syringe pump at 10 μl min⁻¹. This flow rate was maintained for the entirety of the analysis.

For every potentiostatic Co L₃- and O K-edge measurement, about 2 and 5 min long replicate scans were recorded, respectively, at each sample spot for all datasets. For Co L₃-edge, the number of spectra recorded were $n_{1.75\text{V}} = 6$, $n_{1.80\text{V}} = 8$, $n_{1.85\text{V}} = 7$, $n_{1.90\text{V}} = 5$, $n_{2.00\text{V}} = 13$, $n_{2.05\text{V}} = 8$ and $n_{2.10\text{V}} = 7$. Additional spectra were taken on different sample spots to ensure no detectable contribution of beam effects. The spectra were fully reproducible when repeating the applied potential sequence.

Fixed energy X-ray absorption voltammetry (FEXRAV) data at the Co K-edge were acquired using the same spectroelectrochemical set-up as for the steady-state measurements described above. The photon energy was fixed at 7,700; 7,710; 7,720; 7,725 and 8,000 eV and the resultant TFY was collected using the potential scan rates of 0.005, 0.010, 0.020, 0.040 and 0.060 V s⁻¹. The TFY signal was collected at a rate of one data point per second for all energies and potential scan rates measured yielding one TFY data point per 0.005, 0.01, 0.02, 0.04 and 0.06 V. The Co L₃- and O K-edge FEXRAV data were acquired similarly, in the same measurement geometry as used for the Co L₃- and O K-edge steady-state experiments. The photon energy was fixed at 775.0, 780.75 and 782.9 eV for the Co L₃-edge FEXRAV measurements and at 527.0, 530.0 and 531.2 eV for the O K-edge FEXRAV measurements. The TFY signal was collected at a rate of one data point per second while cycling the potential with a scan rate of 0.005 V s⁻¹, yielding one TFY data point per 0.005 V. For both hard and soft XAS, the spectroscopic data collection and electrochemical data collection were aligned within an accuracy of about ± 0.5 s. At least three cycles were recorded for every photon energy, which were fully reproducible. Whenever required, FEXRAV data were corrected for changes in baseline intensity (TFY_{corr}) following a documented procedure⁴², where the TFY_{raw} values are divided by the linearisation of the TFY_{raw} baseline (M_{TFY}) and then multiplied by the final TFY_{raw} value recorded (equation (1)).

$$\text{TFY}_{\text{corr}} = \frac{\text{TFY}_{\text{raw}}}{M_{\text{TFY}}} \times \text{TFY}_{\text{final}} \quad (1)$$

First principles simulations

The Co L-edge spectra of Co ions in the bulk were computed at the ligand field theory level using the Quanty package⁵⁴ and parameters provided in the caption of Supplementary Fig. 22. The Pb(Co)O₂ surface species were computed using a combined density functional theory and Bethe–Salpeter equation approach. All simulations were done on four-layer slabs of (110) terminated of β-PbO₂ with half of the coordinatively unsaturated Pb sites on the surface substituted with Co. Surface phase diagrams were computed using the computational hydrogen electrode⁵⁵ by considering H₂O, OH, O, OOH and OO adsorbed on the substitutional cobalt atoms and H on the surface oxygen sites. Geometries were found by relaxing the top two layers of the slabs using the Quantum ESPRESSO package^{56,57}, with the PBE exchange and correlation potential⁵⁸ together with a 3 eV on-site Hubbard U term acting on the Co 3d manifold. All simulations were spin polarized. PAW datasets from the PS library⁵⁹ were employed using a kinetic energy (charge density) cut-off of 60 Ry (600 Ry). A (4 × 4) k-point mesh was used for the (1 × 2) surface with cold smearing⁶⁰ using a smearing parameter of 0.01 Ry. Periodic images were separated by about 15 Å of vacuum. XA spectra were computed for the relaxed surfaces by solving the Bethe–Salpeter equation for the core level absorption^{61–63}, with the OCEAN package^{64,65}, coupled to Quantum ESPRESSO using norm-conserving pseudopotentials with a kinetic energy cut-off of 120 Ry. Empty states were included up to about 100 eV above the threshold. All other parameters matched those used for geometry relaxation. Relative XAS alignment was accomplished using the ΔSCF procedure⁶⁶. Powder spectra are reported, which were computed as the trace of the atomic absorption tensors, with a lifetime broadening of 0.5 eV (ref. 67).

Data availability

The authors declare that all data supporting the findings of this study are available within the paper and Supplementary Information files. Source data are provided with this paper.

References

- Kibsgaard, J. & Chorkendorff, I. Considerations for the scaling-up of water splitting catalysts. *Nat. Energy* **4**, 430–433 (2019).
- Pham, C. V., Escalera-López, D., Mayrhofer, K., Cherevko, S. & Thiele, S. Essentials of high performance water electrolyzers—from catalyst layer materials to electrode engineering. *Adv. Energy Mater.* **11**, 2101998 (2021).
- Chen, F.-Y., Wu, Z.-Y., Adler, Z. & Wang, H. Stability challenges of electrocatalytic oxygen evolution reaction: from mechanistic understanding to reactor design. *Joule* **5**, 1704–1731 (2021).
- Li, A. et al. Enhancing the stability of cobalt spinel oxide towards sustainable oxygen evolution in acid. *Nat. Catal.* **5**, 109–118 (2022).
- Cao, J., Zhang, D., Ren, B., Song, P. & Xu, W. Tungsten single atoms incorporated in cobalt spinel oxide for highly efficient electrocatalytic oxygen evolution in acid. *Energy Environ. Sci.* **17**, 5911–5921 (2024).
- Chong, L. et al. La- and Mn-doped cobalt spinel oxygen evolution catalyst for proton exchange membrane electrolysis. *Science* **380**, 609–616 (2023).
- Tran-Phu, T. et al. Nanoscale TiO₂ coatings improve the stability of an Earth-abundant cobalt oxide catalyst during acidic water oxidation. *ACS Appl. Mater. Interfaces* **14**, 33130–33140 (2022).
- Ta, X. M. C. et al. Optimal coatings of Co₃O₄ anodes for acidic water electrooxidation. *Small* **20**, 2304650 (2023).
- Moreno-Hernandez, I. A. et al. Crystalline nickel manganese antimonate as a stable water-oxidation catalyst in aqueous 1.0 M H₂SO₄. *Energy Environ. Sci.* **10**, 2103–2108 (2017).
- Luke, S. et al. Mixed metal–antimony oxide nanocomposites: low pH water oxidation electrocatalysts with outstanding durability at ambient and elevated temperatures. *J. Mater. Chem. A* **9**, 27468–27484 (2021).
- Du, H.-L. et al. Durable electrooxidation of acidic water catalysed by a cobalt-bismuth-based oxide composite: an unexpected role of the F-doped SnO₂ substrate. *ChemCatChem* **14**, e202200013 (2022).
- Luke, S. et al. High performance acidic water electrooxidation catalysed by manganese-antimony oxides promoted by secondary metals. *EES Catalysis* **1**, 730–741 (2023).
- Ram, R. et al. Water-hydroxide trapping in cobalt tungstate for proton exchange membrane water electrolysis. *Science* **384**, 1373–1380 (2024).
- Geiger, S. et al. The stability number as a metric for electrocatalyst stability benchmarking. *Nat. Catal.* **1**, 508–515 (2018).
- Bloor, L. G., Molina, P. I., Symes, M. D. & Cronin, L. Low pH electrolytic water splitting using Earth-abundant metastable catalysts that self-assemble in situ. *J. Am. Chem. Soc.* **136**, 3304–3311 (2014).
- Chatti, M. et al. Intrinsically stable in situ generated electrocatalyst for long-term oxidation of acidic water at up to 80 °C. *Nat. Catal.* **2**, 457–465 (2019).
- Bonke, S. A. et al. Electrolysis of natural waters contaminated with transition-metal ions: identification of a metastable FePb-based oxygen-evolution catalyst operating in weakly acidic solutions. *ChemPlusChem* **83**, 704–710 (2018).
- Thorarinsdottir, A. E., Costentin, C., Veroneau, S. S. & Nocera, D. G. p-Block metal oxide noninnocence in the oxygen evolution reaction in acid: the case of bismuth oxide. *Chem. Mater.* **34**, 826–835 (2022).
- Simondson, D. et al. Stable acidic water oxidation with a cobalt–iron–lead oxide catalyst operating via a cobalt-selective self-healing mechanism. *Angew. Chem. Int. Ed.* **60**, 15821–15826 (2021).
- Wang, J. et al. Heterostructure boosts a noble-metal-free oxygen-evolving electrocatalyst in acid. *Energy Environ. Sci.* **17**, 5972–5983 (2024).
- Risch, M. et al. Water oxidation by amorphous cobalt-based oxides: in situ tracking of redox transitions and mode of catalysis. *Energy Environ. Sci.* **8**, 661–674 (2015).
- King, H. J. et al. Photon-induced, timescale, and electrode effects critical for the in situ X-ray spectroscopic analysis of electrocatalysts: the water oxidation case. *J. Phys. Chem. C* **123**, 28533–28549 (2019).
- Liu, S. et al. Phosphate coordination in a water-oxidizing cobalt oxide electrocatalyst revealed by X-ray absorption spectroscopy at the phosphorus K-edge. *Catalysts* **13**, 1151 (2023).
- Mohammadi, M. R. et al. Exploring the limits of self-repair in cobalt oxide films for electrocatalytic water oxidation. *ACS Catal.* **10**, 7990–7999 (2020).
- Liu, S. et al. Electrocatalytic water oxidation at neutral pH—deciphering the rate constraints for an amorphous cobalt-phosphate catalyst system. *Adv. Energy Mater.* **12**, 2202914 (2022).
- Pfeifer, V. et al. The electronic structure of iridium oxide electrodes active in water splitting. *Phys. Chem. Chem. Phys.* **18**, 2292–2296 (2016).
- Pfeifer, V. et al. In situ observation of reactive oxygen species forming on oxygen-evolving iridium surfaces. *Chem. Sci.* **8**, 2143–2149 (2017).
- Spanos, I. et al. Standardized benchmarking of water splitting catalysts in a combined electrochemical flow cell/inductively coupled plasma–optical emission spectrometry (ICP-OES) setup. *ACS Catal.* **7**, 3768–3778 (2017).
- Papakonstantinou, G., Spanos, I., Dam, A. P., Schlögl, R. & Sundmacher, K. Electrochemical evaluation of the de-/re-activation of oxygen evolving Ir oxide. *Phys. Chem. Chem. Phys.* **24**, 14579–14591 (2022).
- Zhang, Y., Simonov, A. N., Zhang, J. & Bond, A. M. Fourier transformed alternating current voltammetry in electromaterials research: direct visualisation of important underlying electron transfer processes. *Curr. Opin. Electrochem.* **10**, 72–81 (2018).
- Knöppel, J. et al. On the limitations in assessing stability of oxygen evolution catalysts using aqueous model electrochemical cells. *Nat. Comm.* **12**, 2231 (2021).
- Risch, M. et al. Cobalt–oxo core of a water-oxidizing catalyst film. *J. Am. Chem. Soc.* **131**, 6936–6937 (2009).
- Hausmann, J. N., Mebs, S., Dau, H., Driess, M. & Menezes, P. W. Oxygen evolution activity of amorphous cobalt oxyhydroxides: interconnecting precatalyst reconstruction, long-range order, buffer-binding, morphology, mass transport, and operation temperature. *Adv. Mater.* **34**, 2207494 (2022).
- Hocking, R. K. & Solomon, E. I. in *Molecular Electronic Structures of Transition Metal Complexes I* Vol. 142 (eds Mingos, D. M. P. et al.) 155–184 (Springer, 2012).
- Kerr, B. V. et al. Characterization of energy materials with X-ray absorption spectroscopy—advantages, challenges, and opportunities. *Energy Fuels* **36**, 2369–2389 (2022).
- Yoon, W.-S. et al. Oxygen contribution on Li-ion intercalation–deintercalation in LiCoO₂ investigated by O K-edge and Co L-edge X-ray absorption spectroscopy. *J. Phys. Chem. B* **106**, 2526–2532 (2002).
- Bonke, S. A., Bond, A. M., Spiccia, L. & Simonov, A. N. Parameterization of water electrooxidation catalyzed by metal oxides using Fourier transformed alternating current voltammetry. *J. Am. Chem. Soc.* **138**, 16095–16104 (2016).

38. Hodgetts, R. Y., Du, H.-L., Nguyen, T. D., MacFarlane, D. & Simonov, A. N. Electrocatalytic oxidation of hydrogen as an anode reaction for the Li-mediated N_2 reduction to ammonia. *ACS Catal.* **12**, 5231–5246 (2022).
39. Simondson, D. et al. Mixed silver–bismuth oxides: a robust oxygen evolution catalyst operating at low pH and elevated temperatures. *ACS Catal.* **12**, 12912–12926 (2022).
40. Snitkoff-Sol, R. Z., Rimón, O., Bond, A. M. & Elbaz, L. Direct measurement of the oxygen reduction reaction kinetics on iron phthalocyanine using advanced transient voltammetry. *Nat. Catal.* **7**, 139–147 (2024).
41. Frydendal, R. et al. Benchmarking the stability of oxygen evolution reaction catalysts: the importance of monitoring mass losses. *ChemElectroChem* **1**, 2075–2081 (2014).
42. Pasquini, C. et al. Operando tracking of oxidation-state changes by coupling electrochemistry with time-resolved X-ray absorption spectroscopy demonstrated for water oxidation by a cobalt-based catalyst film. *Anal. Bioanal. Chem.* **413**, 5395–5408 (2021).
43. Minguzzi, A. et al. Fixed energy X-ray absorption voltammetry. *Anal. Chem.* **85**, 7009–7013 (2013).
44. Tesch, M. F. & Simonov, A. N. Tracking the transient: real-time exploration of electromaterials by dynamic single energy X-ray spectroelectrochemistry. *Curr. Opin. Electrochem* **35**, 101038 (2022).
45. Mizokawa, T. et al. Role of oxygen holes in Li_xCoO_2 revealed by soft X-ray spectroscopy. *Phys. Rev. Lett.* **111**, 056404 (2013).
46. Liu, J. et al. Efficient and stable proton exchange membrane water electrolysis enabled by stress optimization. *ACS Cent. Sci.* **10**, 852–859 (2024).
47. Tesch, M. F. et al. Vacuum compatible flow-cell for high-quality in situ and operando soft X-ray photon-in–photon-out spectroelectrochemical studies of energy materials. *Electrochem. Sci. Adv.* **2**, e2100141 (2022).
48. Tesch, M. F. et al. Evolution of oxygen–metal electron transfer and metal electronic states during manganese oxide catalyzed water oxidation revealed with in situ soft X-ray spectroscopy. *Angew. Chem. Int. Ed.* **58**, 3426–3432 (2019).
49. Glover, C. et al. Status of the X-ray absorption spectroscopy (XAS) beamline at the Australian synchrotron. *AIP Conf. Proc.* **882**, 884–886 (2007).
50. Kappen, P. & Ruben, G. AS-VerSI, ver. 0.2.1, Computer Program, Sakura: Data Explorer for X-ray Absorption Spectroscopy (XAS) Data (Australian Synchrotron, 2013).
51. Ravel, B. & Newville, M. ATHENA, ARTEMIS, HEPHAESTUS: data analysis for X-ray absorption spectroscopy using IFEFFIT. *J. Synchrotron Radiat.* **12**, 537–541 (2005).
52. Tenderholt, A., Hedman, B. & Hodgson, K. O. PySpline: a modern, cross-platform program for the processing of raw averaged XAS edge and EXAFS data. *AIP Conf. Proc.* **882**, 105–107 (2007).
53. Aziz, E. F., Xiao, J., Golnak, R. & Tesch, M. LiXEdrom: high energy resolution RIXS station dedicated to liquid investigation at BESSY II. *J. Large-Scale Res. Facil.* **2**, A80 (2016).
54. Haverkort, M. W., Zwierzycki, M. & Andersen, O. K. Multiplet ligand-field theory using Wannier orbitals. *Phys. Rev. B* **85**, 165113 (2012).
55. Nørskov, J. K. et al. Origin of the overpotential for oxygen reduction at a fuel-cell cathode. *J. Phys. Chem. B* **108**, 17886–17892 (2004).
56. Giannozzi, P. et al. QUANTUM ESPRESSO: a modular and open-source software project for quantum simulations of materials. *J. Phys. Condens. Matter* **21**, 395502 (2009).
57. Giannozzi, P. et al. Advanced capabilities for materials modelling with Quantum ESPRESSO. *J. Phys. Condens. Matter* **29**, 465901 (2017).
58. Perdew, J. P., Burke, K. & Ernzerhof, M. Generalized gradient approximation made simple. *Phys. Rev. Lett.* **77**, 3865–3868 (1996).
59. Dal Corso, A. Pseudopotentials periodic table: from H to Pu. *Comput. Mater. Sci.* **95**, 337–350 (2014).
60. Marzari, N., Vanderbilt, D., De Vita, A. & Payne, M. C. Thermal contraction and disordering of the Al(110) surface. *Phys. Rev. Lett.* **82**, 3296–3299 (1999).
61. Shirley, E. L. Ti 1s pre-edge features in rutile: a Bethe–Salpeter calculation. *J. Electron. Spectrosc. Relat. Phenom.* **136**, 77–83 (2004).
62. Abbasi, T. & Abbasi, S. A. ‘Renewable’ hydrogen: prospects and challenges. *Renew. Sustain. Energy Rev.* **15**, 3034–3040 (2011).
63. Soininen, J. A. & Shirley, E. L. Scheme to calculate core hole–electron interactions in solids. *Phys. Rev. B* **64**, 165112 (2001).
64. Vinson, J. & Rehr, J. J. Ab initio Bethe–Salpeter calculations of the X-ray absorption spectra of transition metals at the L-shell edges. *Phys. Rev. B* **86**, 195135 (2012).
65. Vinson, J., Rehr, J. J., Kas, J. J. & Shirley, E. L. Bethe–Salpeter equation calculations of core excitation spectra. *Phys. Rev. B* **83**, 115106 (2011).
66. Pehlke, E. & Scheffler, M. Evidence for site-sensitive screening of core holes at the Si and Ge (001) surface. *Phys. Rev. Lett.* **71**, 2338–2341 (1993).
67. Krause, M. O. & Oliver, J. H. Natural widths of atomic K and L levels, K_α X-ray lines and several KLL Auger lines. *J. Phys. Chem. Ref. Data* **8**, 329–338 (1979).

Acknowledgements

This study was financially supported by the Australian Research Council (Future Fellowships to A.N.S. and R.K.H.; FF200100317 and FT230100054), Office of Naval Research Global (number N62909-23-1-2051), Australian Renewable Energy Agency (project 2018-RND008) and Deutscher Akademischer Austauschdienst (DAAD; project 57511800). D.S. gratefully acknowledges the support from the R. Tait and J. Tait Postgraduate Research Scholarship. M.F.T. and A.N.S. are grateful for funding within the German BMBF cluster project ‘PrometH₂eus’ (FKZ 03HY105E). B.J. is supported by a Fellowship at the University of Wollongong. A.N.S. is also grateful to the support from Monash University through the Research Talent Accelerator programme. Parts of this research were undertaken at the XAS beamline of the Australian Synchrotron (ANSTO), LiXEdrom station at the U49-2 PGM-1 of the BESSY II synchrotron facility (Berlin, Germany), Monash Centre of Electron Microscopy and Monash X-ray Platform. We thank the Australian Synchrotron and the Helmholtz-Zentrum Berlin für Materialien und Energie for the allocation of synchrotron radiation beamtime, the Los Alamos National Laboratory Institutional Computing Program for high-performance computing resources, and M. R. Rizk (Monash University) for assistance in the design of the PEMWE test station.

Author contributions

D.S. co-designed experiments, undertook major experiments (electrochemical, FTacv, hard and soft XAS, eQCM, XPS, SEM), analysed data and co-wrote the manuscript. M.F.T. and A.N.S. conceived of and designed the project, co-designed experiments, analysed data and co-wrote the manuscript. M.F.T. also undertook soft XAS measurements. I.S. co-designed and undertook eQCM studies. T.E.J. designed and undertook first principles calculations. J.G. undertook PEMWE and inductively coupled plasma mass spectrometric experiments. B.V.K., M.C. and B.J. supported the hard XAS studies. S.A.B. supported the FTacv experiments and contributed to data interpretations. R.G. and J.X. supported the soft XAS studies. D.R.M. contributed to data interpretations and manuscript preparation. R.K.H. co-designed hard and soft XAS studies, analysed data and contributed to manuscript preparation. A.N.S. supervised the project.

Funding

Open access funding provided by Monash University.

Competing interests

The authors declare no competing interests.

Additional information

Supplementary information The online version contains supplementary material available at <https://doi.org/10.1038/s41560-025-01812-x>.

Correspondence and requests for materials should be addressed to Marc F. Tesch, Rosalie K. Hocking or Alexandr N. Simonov.

Peer review information *Nature Energy* thanks Yuanyue Liu and the other, anonymous, reviewers for their contribution to the peer review of this work.

Reprints and permissions information is available at www.nature.com/reprints.

Publisher's note Springer Nature remains neutral with regard to jurisdictional claims in published maps and institutional affiliations.

Open Access This article is licensed under a Creative Commons Attribution 4.0 International License, which permits use, sharing, adaptation, distribution and reproduction in any medium or format, as long as you give appropriate credit to the original author(s) and the source, provide a link to the Creative Commons licence, and indicate if changes were made. The images or other third party material in this article are included in the article's Creative Commons licence, unless indicated otherwise in a credit line to the material. If material is not included in the article's Creative Commons licence and your intended use is not permitted by statutory regulation or exceeds the permitted use, you will need to obtain permission directly from the copyright holder. To view a copy of this licence, visit <http://creativecommons.org/licenses/by/4.0/>.

© The Author(s) 2025